THE ASTROPHYSICAL JOURNAL, 380:212–222, 1991 October 10

EFFECTS OF ABERRATION AND ADVECTION ON LINE FORMATION

A. PERAIAH
Indian Institute of Astrophysics, Bangalore 560034, India
Received 1990 April 18; accepted 1991 April 12

ABSTRACT

We studied the effects of inclusion of the aberration and advection terms in the equation of the line transfer. We have considered spherical shells whose ratios of outer (B) to inner (A) radii (B/A) are 2, 5, and 10 and with line-center optical depths 500, 1300, and 1350. The velocities of expansion of the medium are set at 1000, 2000, 3000, 4000, and 5000 km s^{-1}. We calculated the line source functions and the corresponding profiles of lines. We have considered the individual and combined effects of the transverse and radial velocity gradients, and those of aberration and advection in plane-parallel and spherically symmetric geometries on the line source functions and the emerging line profiles. It is found that large effects are generated in the radiation field when these physical mechanisms are taken into account in the transfer of line radiation. We tested the method for various velocity laws and found it to be stable.

Subject headings: line formation — radiative transfer — stars: circumstellar shells — stars: supernovae

1. INTRODUCTION

In an earlier paper (Peraiah 1987, hereafter Paper I) we found that in a plane-parallel and coherently scattering medium moving with velocities of the order of γ ($=v/c$, where v is the velocity of the gas and c is the velocity of light) equal to 0.017, the mean intensities of the monochromatic radiation field change considerably when aberration and advection are included in the solution self-consistently. Therefore, it is not unreasonable to expect that aberration and advection will affect the formation of spectral lines.

In the equation of transfer we concentrate on the effect of two types of terms: (1) aberration and advection and (2) comoving frame Doppler shift terms. The gas velocity that appears in the aberration and advection terms is measured in terms of the velocity of light, and the gas velocity that appears in the comoving frame terms is measured in units of mean thermal velocity ($v_{\rm th}$). Here we have to consider the relative importance of these two types of terms. The velocity terms in the aberration and advection terms are substantially smaller than those in comoving frame terms. However, as gas temperature increases, the mean thermal velocity increases and γ in aberration and advection remains unchanged.

We intend to show that in a high-temperature medium in spherical geometry, the aberration and advection terms produce noticeable changes in the emerging line profiles. We have chosen a purely scattering isothermal medium in which no thermal emission occurs.

2. SOLUTION OF THE TRANSFER EQUATION

The equation of transfer in the comoving frame of the fluid with the aberration and advection terms is written as (see Mihalas, Kunasz, & Hummer 1976)

$$(\mu_0+\gamma)\frac{\partial U(r,\mu_0,x)}{\partial r}+\frac{1-\mu_0^2}{r}\left[1+\mu_0\gamma\left(1-\frac{r}{\gamma}\frac{d\gamma}{dr}\right)\right]\frac{\partial U(r,\mu_0,x)}{\partial \mu_0}+\left\{3\left[\frac{\gamma}{r}(1-\mu_0^2)+\mu_0^2\frac{d\gamma}{dr}\right]-\frac{2(\mu_0+\gamma)}{r}\right\}U(r,\mu_0,x)$$
$$=\left[\frac{v'}{r}(1-\mu_0^2)+\mu_0^2\frac{dv'}{dr}\right]\frac{\partial U(r,\mu_0,x)}{\partial x}+K(r)[S(r,x)-U(r,\mu_0,x)]\,,\qquad \text{for}\quad 0<\mu\le 1 \quad (1)$$

and

$$-(\mu_0+\gamma)\frac{\partial U(r,-\mu_0,x)}{\partial r}-\frac{1-\mu_0^2}{r}\left[1-\mu_0\gamma\left(1-\frac{r}{\gamma}\frac{d\gamma}{dr}\right)\right]\frac{\partial U(r,-\mu_0,x)}{\partial \mu_0}+\left\{3\left[\frac{\gamma}{r}(1-\mu_0^2)+\mu_0^2\frac{d\gamma}{dr}\right]-\frac{2(\gamma+\mu_0)}{r}\right\}U(r,-\mu_0,x)$$
$$=\left[\frac{v'}{r}(1-\mu_0^2)+\mu_0^2\frac{dv'}{dr}\right]\frac{\partial U(r,-\mu_0,x)}{\partial x}+K(r)[S(r,x)-U(r,-\mu_0,x)]\,,\qquad \text{for}\quad -1\le\mu<0\,, \quad (2)$$

where $v'=v/v_{\rm th}$ is the velocity of the gas in terms of the mean thermal units and $\gamma=v/c$, where c is the velocity of light. The quantity $U(r,\mu_0,x)$ is given by

$$U(r,\mu_0,x)=4\pi r^2 I(r,\mu_0,x)\,, \quad (3a)$$

where $I(r,\mu_0,x)$ is the specific intensity. Furthermore,

$$\mu_0=\frac{\mu-\gamma}{1-\mu\gamma}\,, \quad (3b)$$

μ being the cosine of the angle made by the ray with the radius vector. Here $K(r,x,\mu_0)$ is the absorption coefficient given by (see

Grant & Peraiah 1972, hereafter GP)

$$K(r, x, \mu_0) = K_L[\beta + \phi(r, x, \mu_0)] , \tag{4}$$

and $S(x, \mu_0, r)$ is the source function given by

$$S(x, \mu_0, r) = \frac{\phi(x, \mu_0, r)S_L(r) + \beta S_c(r)}{\beta + \phi(x, \mu_0, r)} , \tag{5}$$

where $x = (\nu - \nu_0)/\Delta\nu_D$, where $\Delta\nu_D$ is the Doppler width. $S_c(r)$ is the continuum source function given by

$$S_c(r) = \sigma' B(T(r)) , \qquad B(T(r)) = 4\pi r^2 b(T(r)) , \tag{6}$$

where σ' is a parameter which we intend to specify in advance. The quantity S_L is the line source function, given by

$$S_L(r) = \frac{1-\epsilon}{2} \int_{-\infty}^{+\infty} \int_{-1}^{+1} \phi(x', \mu_0, r)U(x', \mu_0, r)dx'd\mu_0' + \epsilon B(T(r)) ; \tag{7}$$

$\phi(x, \mu_0, r)$ is the profile function of the line, $b(T(r))$ is the Planck function, ϵ is the probability of a photon being thermalized per scatter by collisional de-excitation, and β is the ratio of continuum to line absorption coefficient. The quantity K_L is the line center absorption coefficient.

We solve equations (1) and (2) by following the procedure described in GP. The discrete equations (1) and (2) are written

$$\boldsymbol{M}_0^+(\boldsymbol{U}_{n+1}^+ - \boldsymbol{U}_n^+) + \rho_c(\boldsymbol{\Lambda}'_+\boldsymbol{U}_{n+1/2}^+ + \boldsymbol{\Lambda}'_-\boldsymbol{U}_{n+1/2}^-) + [\tau_{n+1/2}\boldsymbol{\Phi}_{n+1/2} + 3\gamma\rho_c(\boldsymbol{M}_0^1 + \Delta\gamma\boldsymbol{M}_0^2) - 2\rho_c(\boldsymbol{M}_0 + \gamma\boldsymbol{I})]\boldsymbol{U}_{n+1/2}^+$$
$$= \tau_{n+1/2}\boldsymbol{S}_{n+1/2} + \tfrac{1}{2}(1-\epsilon)\tau_{n+1/2}(\boldsymbol{\Phi}\boldsymbol{\Phi}^T\boldsymbol{W})(\boldsymbol{U}_{n+1/2}^+ + \boldsymbol{U}_{n+1/2}^-) + \boldsymbol{M}_1\boldsymbol{d}\boldsymbol{U}_{n+1/2}^+ , \tag{8}$$

$$\boldsymbol{M}_0^-(\boldsymbol{U}_n^- - \boldsymbol{U}_{n+1}^-) - \rho_c(\boldsymbol{\Lambda}'_+\boldsymbol{U}_{n+1/2}^- + \boldsymbol{\Lambda}'_-\boldsymbol{U}_{n+1/2}^+) + [\tau_{n+1/2}\boldsymbol{\Phi}_{n+1/2} + 3\gamma\rho_c(\boldsymbol{M}_0^1 + \Delta\gamma\boldsymbol{M}_0^2) - 2\rho_c(\gamma\boldsymbol{I} - \boldsymbol{M}_0)]\boldsymbol{U}_{n+1/2}^-$$
$$= \tau_{n+1/2}\boldsymbol{S}_{n+1/2} + \tfrac{1}{2}(1-\epsilon)\tau_{n+1/2}(\boldsymbol{\Phi}\boldsymbol{\Phi}^T\boldsymbol{W})(\boldsymbol{U}_{n+1/2}^+ + \boldsymbol{U}_{n+1/2}^-) + \boldsymbol{M}_1\boldsymbol{d}\boldsymbol{U}_{n+1/2}^- , \tag{9}$$

where

$$\boldsymbol{M}_1 = (\boldsymbol{M}^1\Delta v'_{n+1/2} + \boldsymbol{M}^2\rho_c v'_{n+1/2}) , \tag{10}$$

$$\boldsymbol{M}^1 = \begin{pmatrix} \boldsymbol{M}_m^1 & & & \\ & \boldsymbol{M}_m^1 & & \\ & & \boldsymbol{M}_m^1 & \\ & & & \ddots \end{pmatrix}, \qquad \boldsymbol{M}_m^1 = (\mu_j^2\delta_{jl}) , \tag{11}$$

$$\boldsymbol{M}^2 = \begin{pmatrix} \boldsymbol{M}_m^2 & & \\ & \boldsymbol{M}_m^2 & \\ & & \ddots \end{pmatrix}, \qquad \boldsymbol{M}_m^2 = [(1-\mu_j^2)\delta_{jl}] , \tag{12}$$

for $j, l = 1, 2, \ldots, J$, and

$$\Delta v'_{n+1/2} = v'_{n+1} - v'_n . \tag{13}$$

$\boldsymbol{I}$ is the unit matrix; $v'_{n+1/2}$ is the average velocity of the shell in mean thermal units bounded by the radii r_n and r_{n+1}. The matrix $\boldsymbol{d}$ is determined by the condition of flux conservation (see Peraiah 1980a, b) and is given by

$$\boldsymbol{d} = \begin{pmatrix} -d_1 & d_1 & 0 & & & & \\ -d_2 & 0 & d_2 & 0 & & & \\ 0 & -d_3 & 0 & d_3 & 0 & & \\ & & & & & & \\ & & & & & d_{I-1} & \\ & & & & & -d_I & d_I \end{pmatrix}, \tag{14}$$

with

$$d_i = (x_{i+1} - x_{i-1})^{-1} \qquad \text{for } i = 2, 3, 4, \ldots, I-1 , \tag{15}$$

where I is the total number of frequency points. Further,

$$\boldsymbol{M}_0^+ = \begin{pmatrix} \boldsymbol{M}_{0,m}^+ & & & \\ & \boldsymbol{M}_{0,m}^+ & & \\ & & \ddots & \\ & & & \boldsymbol{M}_{0,m}^+ \end{pmatrix}, \qquad \boldsymbol{M}_{0,m}^+ = [(\mu_0 + \gamma)_j]\delta_{jk} , \tag{16}$$

$$M_0^- = \begin{pmatrix} M_{0,m}^- & & & \\ & M_{0,m}^- & & \\ & & \ddots & \\ & & & M_{0,m}^- \end{pmatrix}, \qquad M_{0,m}^- = [(-\mu_0 + \gamma)_j]\delta_{jk}\,, \tag{17}$$

$$M_0 = \begin{pmatrix} M_{0,m} & & & \\ & M_{0,m} & & \\ & & \ddots & \\ & & & M_{0,m} \end{pmatrix}, \qquad M_{0,m} = (\mu_0)_j\,\delta_{jk}\,, \tag{18}$$

$$M_0^1 = \begin{pmatrix} M_{0,m}^1 & & & \\ & M_{0,m}^1 & & \\ & & \ddots & \\ & & & M_{0,m}^1 \end{pmatrix}, \qquad M_{0,m}^1 = [(1 - \mu_0^2)_j]\delta_{jk}\,, \tag{19}$$

$$M_0^2 = \begin{pmatrix} M_{0,m}^2 & & & \\ & M_{0,m}^2 & & \\ & & \ddots & \\ & & & M_{0,m}^2 \end{pmatrix}, \qquad M_{0,m}^2 = (\mu_0^2)_j\,\delta_{jk}\,. \tag{20}$$

By using the diamond scheme (see GP) that

$$U_{n+1/2}^{\pm} = \tfrac{1}{2}(U_n^{\pm} + U_{n+1}^{\pm})\,, \tag{21}$$

we can rewrite equations (8) and (9) as

$$\begin{pmatrix} A_1 & B_1 \\ C_1 & D_1 \end{pmatrix}\begin{pmatrix} U_{n+1}^+ \\ U_n^- \end{pmatrix} = \begin{pmatrix} E_1 & F_1 \\ G_1 & H_1 \end{pmatrix}\begin{pmatrix} U_n^+ \\ U_{n+1}^- \end{pmatrix} + \tau\begin{pmatrix} S_1 \\ S_2 \end{pmatrix}, \tag{22}$$

where

$$A_1 = M_0^+ + \tfrac{1}{2}\rho_c\,\Lambda' + \tfrac{1}{2}\tau\Phi + 3\gamma\rho_c(M_0^1 + \gamma\Delta M_0^2) - 2\rho_c(M_0 + \gamma I) - \tfrac{1}{4}\sigma\tau(\Phi\Phi^T W) - \tfrac{1}{2}M_1\,d, \tag{23}$$

$$B_1 = \tfrac{1}{2}\rho_c\,\Lambda'_- - \tfrac{1}{4}\sigma\tau(\Phi\Phi^T W)\,, \tag{24}$$

$$C_1 = -\tfrac{1}{2}\rho_c\,\Lambda'_- - \tfrac{1}{4}\tau\sigma(\Phi\Phi^T W)\,, \tag{25}$$

$$D_1 = M_0^- - \tfrac{1}{2}\rho_c\,\Lambda'_+ + \tfrac{1}{2}\tau\Phi + 3\gamma\rho_c(M_0^1 + \gamma\Delta M_0^2) - 2\rho_c(I\gamma - M_0) - \tfrac{1}{4}\sigma\tau(\Phi\Phi^T W) - \tfrac{1}{2}M_1\,d\,, \tag{26}$$

$$E_1 = M_0^+ - \tfrac{1}{2}\rho_c\,\Lambda'_+ - [\tfrac{1}{2}\tau\Phi + 3\gamma\rho_c(M_0^1 + \Delta\gamma M_0^2) - 2\rho_c(M_0 + I\gamma)] + \tfrac{1}{4}\tau\sigma(\Phi\Phi^T W) + \tfrac{1}{2}M_1\,d\,, \tag{27}$$

$$F_1 = -\tfrac{1}{2}\rho_c\,\Lambda'_- + \tfrac{1}{4}\tau\sigma(\Phi\Phi^T W)\,, \tag{28}$$

$$G_1 = \tfrac{1}{2}\rho_c\,\Lambda'_- + \tfrac{1}{4}\tau\sigma(\Phi\Phi^T W)\,, \tag{29}$$

$$H_1 = M_0^- + \tfrac{1}{2}\rho_c\,\Lambda'_+ - [\tfrac{1}{2}\tau\Phi + 3\gamma\rho_c(M_0^1 + \Delta\gamma M_0^2) - 2\rho_c(I\gamma + M_0)] + \tfrac{1}{4}\tau\sigma(\Phi\Phi^T W) + \tfrac{1}{2}M_1\,d \tag{30}$$

and $\sigma = 1 - \epsilon$. By setting

$$\Delta^+ = A_1^{-1}\,, \qquad \Delta^- = H_1^{-1}\,, \qquad \Gamma^+ = E_1\,, \qquad \Gamma^- = D_1\,, \tag{31}$$

$$Y_+ = \frac{1}{2}\,\sigma(\Phi\Phi^T W) + \frac{\rho_c}{\tau}\,\Lambda'_-\,, \tag{32}$$

$$Y_- = \frac{1}{2}\,\sigma(\Phi\Phi^T W) - \frac{\rho_c}{\tau}\,\Lambda'_-\,, \tag{33}$$

$$\beta^{+-} = \tfrac{1}{2}\tau\Delta^+ Y_-\,, \tag{34}$$

$$\beta^{-+} = \tfrac{1}{2}\tau\Delta^- Y_+\,, \tag{35}$$

$$\alpha^{+-} = (I - \beta^{+-}\beta^{-+})^{-1}\,, \tag{36}$$

$$\alpha^{-+} = (I - \beta^{-+}\beta^{+-})^{-1}\,, \tag{37}$$

we can write the transmission and reflection matrices as follows:

$$T(n+1, n) = \alpha^{+-}(\Delta^+\Gamma^+ + \beta^{+-}\beta^{-+})\,, \tag{38}$$

$$T(n, n+1) = \alpha^{-+}(\Delta^-\Gamma^- + \beta^{-+}\beta^{+-})\,, \tag{39}$$

$$R(n+1, n) = \alpha^{-+}\beta^{-+}(I + \Delta^+\Gamma^+)\,, \tag{40}$$

$$R(n, n+1) = \alpha^{+-}\beta^{+-}(I + \Delta^-\Gamma^-)\,, \tag{41}$$

and the cell source vectors are given

$$\Sigma^{+}_{n+1/2} = \tau\alpha^{+-}(\Delta^{+} + \beta^{+-}\Delta^{-})S_1 , \tag{42}$$

$$\Sigma^{-}_{n+1/2} = \tau\alpha^{-+}[\Delta^{-} + \beta^{-+}\Delta^{+}]S_2 , \tag{43}$$

where

$$S_1 = S_2 = S_{n+1/2} . \tag{44}$$

3. RESULTS AND DISCUSSION

We employed the transmission and reflection matrices given in equations (38)–(41) to calculate the radiation field. We have not introduced any internal emission and have considered only scattering in the lines. Therefore, we set $\epsilon = 0, \beta = 0$. In this case, the line source function becomes

$$S_L = \frac{1}{2}\int_{-1}^{+1}\int_{-\infty}^{+\infty}\phi(x', \mu_0, r)U(x', \mu_0, r)dx'\,d\mu_0' . \tag{45}$$

We have used a Doppler profile function. Since there are no internal sources, we give the incident radiation as follows:

$$U^{-}(\mu_j, \tau = T, x) = 1.0 , \qquad U^{+}(\mu_j, \tau = 0, x) = 0 , \tag{46}$$

where T is the total optical depth at the line center and $T = \tau_{\max}$. We assume that the density changes as $1/r^2$, and the optical depth is estimated accordingly. We consider the aspect ratio B/A (B = outer radius and A = inner radius of the spherical shell) equal to 2, 5, and 10.

The boundary conditions of the velocity of expansion are given as follows:

$$V(\tau = T, r = A) = 0 , \tag{47}$$

$$V(\tau = 0, r = B) = V , \tag{48}$$

where $V = 0$, 1000, 3000, 4000, and 5000 km s^{-1}. We have presented the results mainly by calculating the line source function S_L given in equation (45). It should be noted here that, while calculating S_L, we have used I instead of U (see eq. [3]). This calculation is done automatically in every shell using the corresponding radius.

When aberration and advection are not considered, the Doppler radial velocity gradients become operative in plane-parallel geometry, while two more additional effects due to transverse velocity gradients and curvature become important. We would like to calculate the effects due to these phenomena together with aberration and advection on the line source function given in equation (45) with the boundary conditions (46), (47), and (48).

In Figure 1 the source function given in equation (45) is plotted for an isothermal medium whose temperature is 30,000 K. The total line-center optical depth is taken to be 1300 in a plane-parallel medium ($B/A = 1$). We have employed the velocities with the boundary condition given in equations (47) and (48). These boundary conditions introduce velocity gradients both in plane-parallel and spherical geometries. The broken curves represent the source functions corresponding to the Doppler velocity gradients without aberration and advection. In plane-parallel geometry, transverse velocity gradients do not exist (as $r \to \infty$, $v/r \to 0$) but radial velocity gradients do exist (see eqs. [1] and [2]). We have introduced the aberration and advection terms into the transfer equation in plane-parallel approximation. The terms of aberration and advection namely, the first term on the left-hand side [i.e., $(\mu_0 + \gamma)\partial U/\partial r$ and the term $3\mu_0^2(d\gamma/dr)U$ on the right-hand side of equation (1) together introduce more effects than those produced by the radial velocity gradient terms, $\mu_0^2(dV'/dr)\partial U/\partial x$]. The changes introduced by the presence of the former two terms are shown by the three continuous curves for 1000, 3000, and 5000 km s^{-1} (44 mtu, $\gamma = 0.003$; 132 mtu, $\gamma \approx 0.01$; 220 mtu, $\gamma \approx 0.017$, respectively). In plane-parallel layers, the interaction of the Doppler-shifted radiation with that of the continuum radiation is very effective in changing the line source function. The velocity field produces Doppler shift and aberration of photons and gives rise to advection which describes "sweeping off" of radiation by the moving fluid. It is the combination of these effects that reduces the source function considerably, as shown by the continuous curves in Figure 1.

We have repeated the calculations for the same parameters given in Figure 1 in the spherical case with $B/A = 10$ and presented these results in Figure 2. Spherical symmetry introduces two effects due to curvature and transverse velocity gradients, and these are represented by the terms $[(1 - \mu_0^2)/r]\partial U/\partial\mu_0$ and $(1 - \mu_0^2)(V'/r)\partial U/\partial x$, respectively, in the transfer equation. The broken curves represent again the effects due to the transverse and radial velocity gradients in the spherical case together with the curvature effect without aberration and advection effects. We see that the effects of sphericity and transverse velocity gradients are to reduce the line source function. In addition to these terms, the terms due to aberration and advection represented by the expressions

$$(\mu_0 - \gamma)\frac{\partial U}{\partial r} , \qquad \frac{1 - \mu_0^2}{r}\mu_0\gamma\left(1 - \frac{r}{\gamma}\frac{d\gamma}{dr}\right)\frac{\partial u}{\partial\mu_0} , \qquad \left\{3\left[\frac{\gamma}{r}(1 - \mu_0^2) + \mu_0^2\frac{d\gamma}{dr}\right] - 2\left(\frac{\mu_0 + \gamma}{r}\right)\right\}U \tag{49}$$

are introduced in the transfer equation. The combined effects of sphericity, Doppler velocity gradients, and the aberration and advection again reduce the source function considerably, as can be seen by the continuous curves in Figure 2. At the surface, the probability of escape increases in the spherical case and dominates the interception of continuum radiation by the Doppler-shifted line. The velocity increases outward (see eqs. [47] and [48]), and because of the effect of advection, the radiation is swept off by the moving matter. This further increases the probability of escape of photons. In the absence of any source to replenish the photons (no

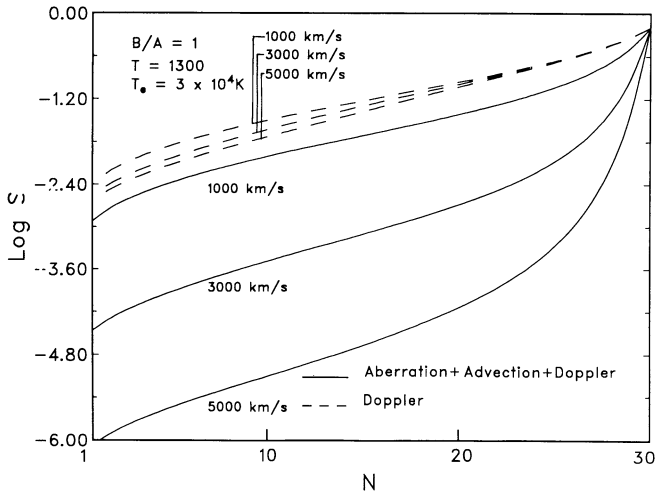

FIG. 1

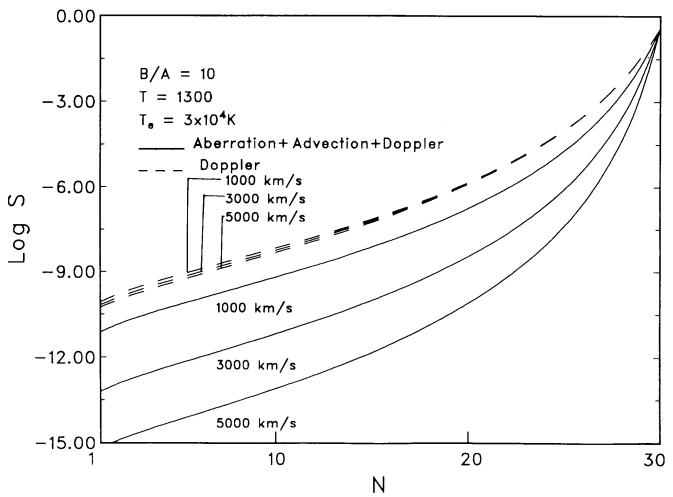

FIG. 2

FIG. 1.—The quantity log S is plotted against the shell numbers in plane-parallel geometry. The broken curves represent the variation of the source function for Doppler velocity gradients, and the continuous curves represent those which include Doppler gradients aberration and advection effects.

FIG. 2.—Same Fig. 1, but for the spherical case with $B/A = 10$.

internal sources are given, since we are dealing only with scattering media), the source function is reduced considerably. Therefore, as shown in Figure 2, for a high velocity of $V = 5000$ km s^{-1} $T = 1300$, and $B/A = 10$, the source function is reduced dramatically as a result of the combination of the effects mentioned above. We have always maintained flux conservation (which is used to correct the code also), although the accuracy starts falling at higher velocities. At higher velocities the critical step size becomes small and the number of additions of the shells increases, and this result in increasing the roundoff and truncation errors.

We would like to show that the importance of the terms containing the velocity gradients is dependent on the temperature of the medium. As the gas velocity appears in the transfer equation in units of the mean thermal velocity, the velocity gradient terms will not dominate the effects in a sufficiently high temperature gas, and the terms containing the aberration and advection will be more dominant in changing the radiation field in such a medium. To show that this case, we have selected isothermal media with temperatures of 10,000, 30,000, 50,000, and 100,000 K. We show in Table 1 the mean thermal units (mtu) of the gas velocities corresponding to the temperatures given above. The mean thermal velocities are calculated by assuming a hydrogen medium, using the formula

$$v_{\rm th} = (2kT_e/m_{\rm H})^{1/2} , \tag{50}$$

where T_e is the temperature, $m_{\rm H}$ is the mass of the hydrogen atom, and k is the Boltzmann constant.

At higher temperatures (say around 10^5 K) the aberration and advection terms are more important than those with transverse velocity gradients. We plotted the quantity $\bar{S}$ given by

$$\bar{S} = \frac{S_V - S_0}{S_0} , \tag{51}$$

where S_0 and S_V correspond to the source functions in the media with $V = 0$ and $V > 0$. We considered the velocities of expansion $V = 1000$ km s^{-1} and $V = 5000$ km s^{-1}. These changes are due to the bulk motion, because the advection and aberration terms are unaffected by the temperature changes. As we increase the temperature, the value of the mtu increases and the number of mtu for a given velocity decreases. From the table we see that for a hydrogen atmosphere the mtu change from 76 to 24 when the temperature changes from 10^4 to 10^5 K. Therefore, at a small number of mtu the aberration and advection appear to be more effective. We also notice that any further increase in temperature will not change the source functions considerably. Therefore it appears that

TABLE 1

VELOCITIES MEASURED IN MEAN THERMAL VELOCITIES CALCULATED USING EQUATION (50)

Temperature (K)	Doppler Velocity for Hydrogen (km s^{-1})	Gas Velocity of 1000 km s^{-1} in mtu[a]	Gas Velocity of 5000 km s^{-1} in mtu[b]
10,000.....	13.13	76	381
30,000.....	22.17	44	220
50,000.....	29.36	34	170
100,000.....	41.5	24	120

[a] $\gamma \approx 0.003$.
[b] $\gamma \approx 0.017$.

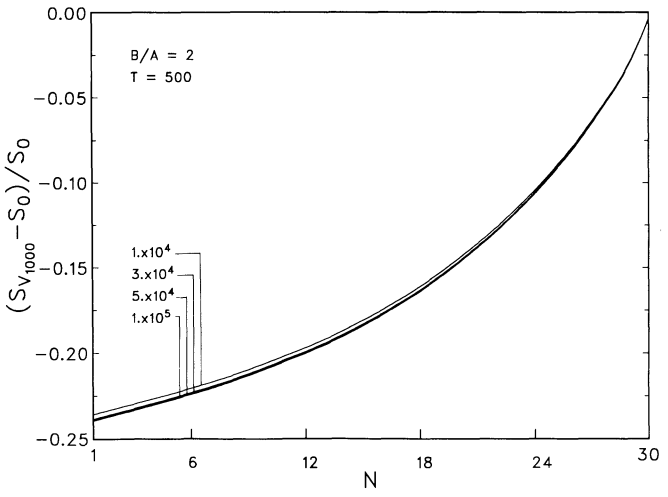

FIG. 3a

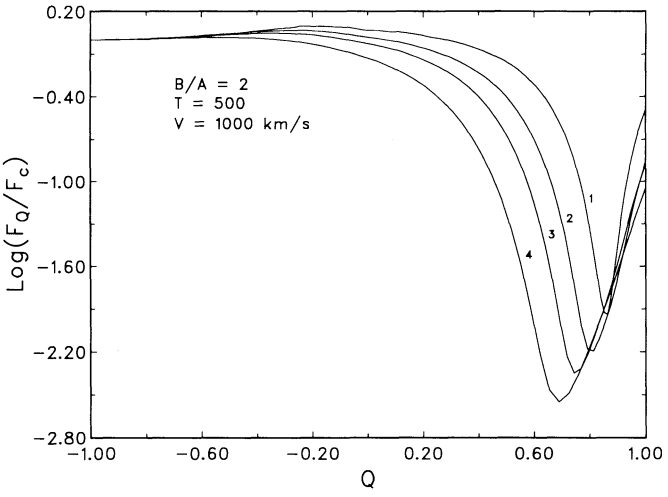

FIG. 3b

FIG. 3.—(*a*) $\bar{S} = (S_\nu - S_0)/S_0$ is plotted against the shell number for temperatures 10^4 K (76 mtu), 3×10^4 K (44 mtu), 5×10^4 K (34 mtu), and 10^5 K (24 mtu). (*b*) Line profiles corresponding to the source function given in (*a*). Numbers on the curves correspond to the temperatures (1) 10^4 K (76 mtu), (2) 3×10^4 K (44 mtu), (3) 5×10^4 K (34 mtu) and (4) 10^5 K (24 mtu).

aberration and advection phenomena dominate even the strong effect of the Doppler velocity gradients. In spherical geometry, when advection exists, the skewing of radiation is more effective. This can be seen from the second term on the left-hand side of equation (1). The curvature term is modified by the extra terms which contain the advection factors. The curvature changes the advection effects through the extra term $[(1 - \mu_0^2)/r]\mu_0 \gamma$. Therefore, it is the combination of aberration, advection, and curvature that dominates the well-known strong effect of the Doppler velocity gradients in the line transfer.

We have already seen that the effects of aberration and advection are pronounced in the case of a monochromatic radiation field (Peraiah 1987) in the plane-parallel approximation and in the spherically symmetric shells (Peraiah 1991). In Figure 3*a* we plotted the quantity $\bar{S}$ defined in equation (51). When the velocity of expansion is 1000 km s^{-1}, the differences are between 23% and 24% for temperatures of 10,000, 30,000, 50,000, and 100,000 K. Corresponding line profiles are plotted in Figure 3*b*; we plotted F_Q/F_C as a function of Q, F_Q and F_C being the integrated fluxes at frequency X_Q and in the continuum. The quantity Q is given by

$$Q = \frac{X_Q}{X_{\max}}, \qquad -1 \leq Q \leq 1, \tag{52}$$

where $X_{\max}$ is the normalized frequency in the continuum adjacent to the line. This is obtained as the sum of the bandwidth x and the velocity measured in mtu. This formulation allows us to present all the profiles corresponding to different velocities (see Mihalas, Kunasz, & Hummer 1975) in one figure. It is interesting to note that the cores of the absorption lines formed in hotter media have smaller shifts from the center of the line in the static medium. This is because of the fact that the gas velocity will have a smaller

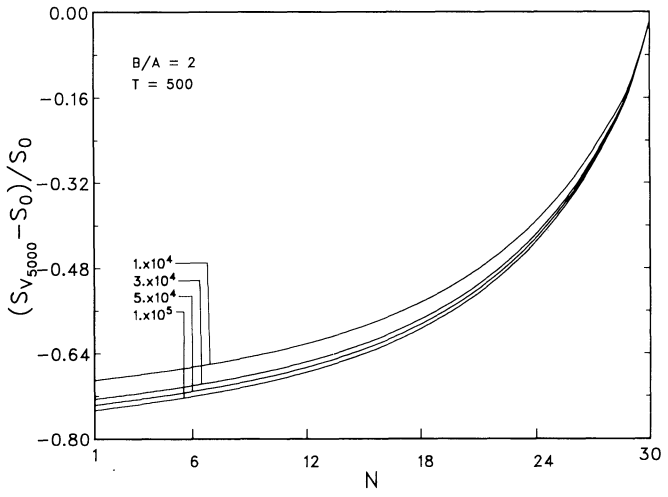

FIG. 4a

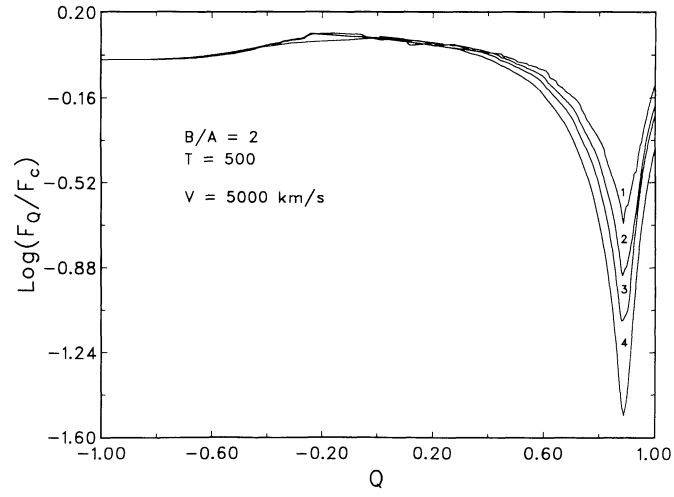

FIG. 4b

FIG. 4.—(*a*) Same as Fig. 3*a*, but for $V = 5000$ km s^{-1}. The temperatures are 10^4 K (381 mtu), 3×10^4 K (220 mtu), 5×10^4 K (170 mtu), and 10^5 K (120 mtu). (*b*) Same as Fig. 3*b*, but for $V = 5000$ km s^{-1}.

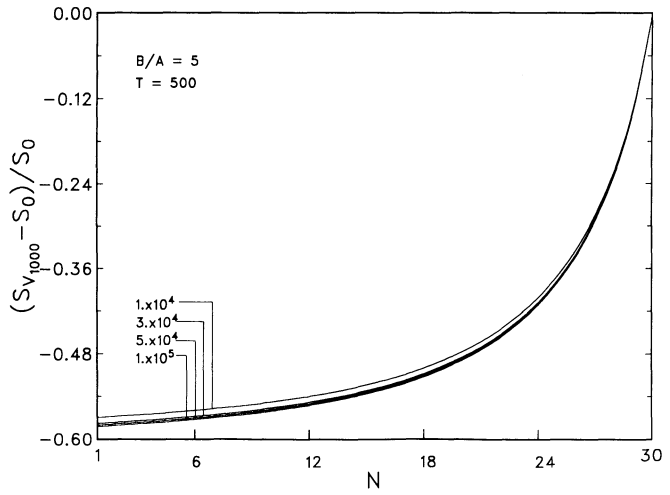

FIG. 5a

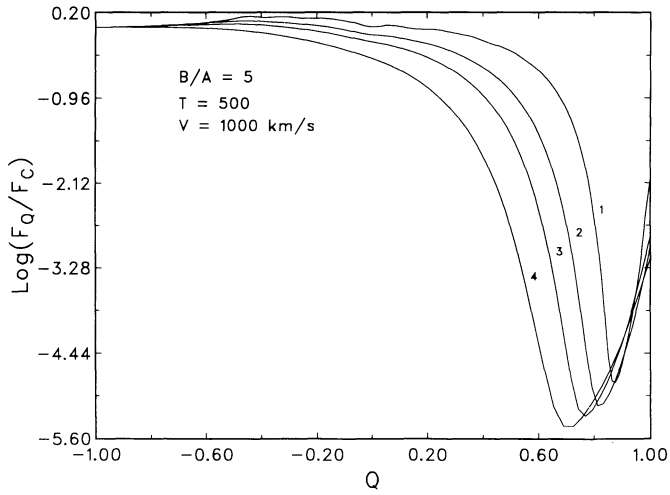

FIG. 5b

FIG. 5.—(*a*) Same as Fig. 3*a*, but for $B/A = 5$. (*b*) Same as Fig. 3*b*, but for $B/A = 5$.

number of mtu in hotter media (as the value of a mean thermal unit increases with the increase in temperature), and the shift of the line center is proportional to the gas velocity measured in mtu.

In Figure 4*a* we plotted $\bar{S}$ for $V = 5000$ km s^{-1} and $B/A = 2$, for the temperatures shown in the figure. We notice that, in contrast to the previous case (see Fig. 3*a*), where $V = 1000$ km s^{-1}, the changes are quite substantial, around 70%, at all the temperatures. At higher temperatures, the differences seem to be enhanced as the aberration and advection terms become more effective as the transverse velocity term measured in mtu becomes smaller. The line profiles corresponding to these source functions are plotted in Figure 4*b*. Interestingly, we notice that the absorption profiles will have core depths proportional to the temperatures. This is due to the fact that as the temperatures increases, the number of mtu decreases and aberration and advection terms increase their effect, which is to reduce the line source function. This results in the removal of more photons from the line center. In Figures 5*a* and 5*b*, we plotted $\bar{S}$ for $V = 1000$ km s^{-1} and the corresponding profiles in Figure 5*b* for $B/A = 5$. These show similar tendencies to those in Figures 3*a* and 3*b*. The change $\bar{S}$ is now around 55% for $V = 1000$ km s^{-1}. This enhanced differences compared to those given in Figure 3*a* are due to the increase in the aspect ratio B/A from 2 to 5. In Figure 6*a* we plotted the $\bar{S}$ corresponding to $V = 5000$ km s^{-1} and $B/A = 5$. We see that the changes in $\bar{S}$ are around 95% for all temperatures. Corresponding profiles are given in Figure 6*b*. These are not similar to those given in Figure 4*b*, which correspond to $V = 5000$ km s^{-1} and $B/A = 2$. When B/A is increased from 2 to 5 and the velocity is increased from $V = 1000$ km s^{-1} to $V = 5000$ km s^{-1}, we get profiles whose absorption cores are deeper with higher temperatures but with different shifts, which are similar to those shown in Figure 5*b*, and the profile becomes narrow.

We would like to find whether the method presented in this paper can be used with different types of velocity laws. For this purpose, we have employed the velocity given in Lucy (1971) and Castor & Lamers (1979), namely,

$$v(r) = v_t\left[1 - (1 - \alpha)\left(\frac{R}{r}\right) - \alpha\left(\frac{R}{r}\right)^2\right]^{1/2} \tag{53}$$

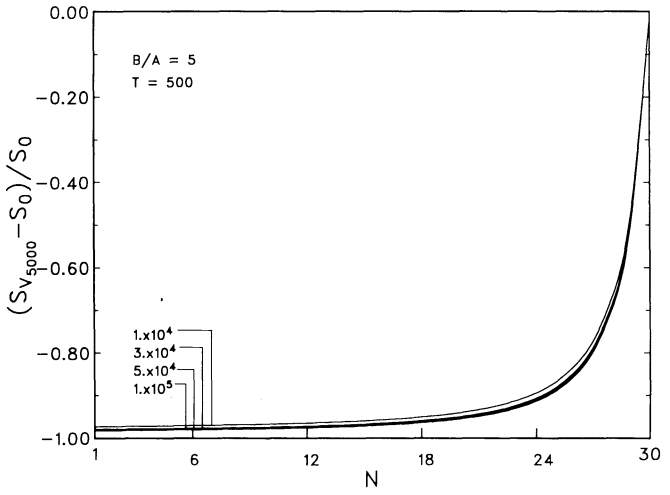

FIG. 6a

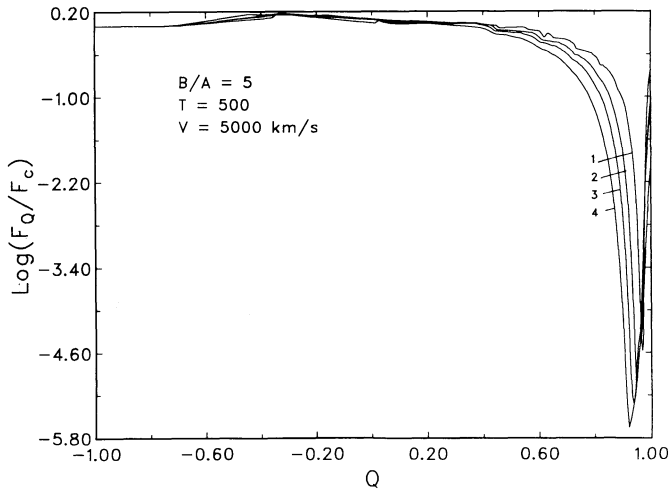

FIG. 6b

FIG. 6.—(*a*) Same as Fig. 3*a*, but for $B/A = 5$ and $V = 5000$ km s^{-1}. (*b*) Same as Fig. 3*b*, but for $B/A = 5$ and $V = 5000$ km s^{-1}.

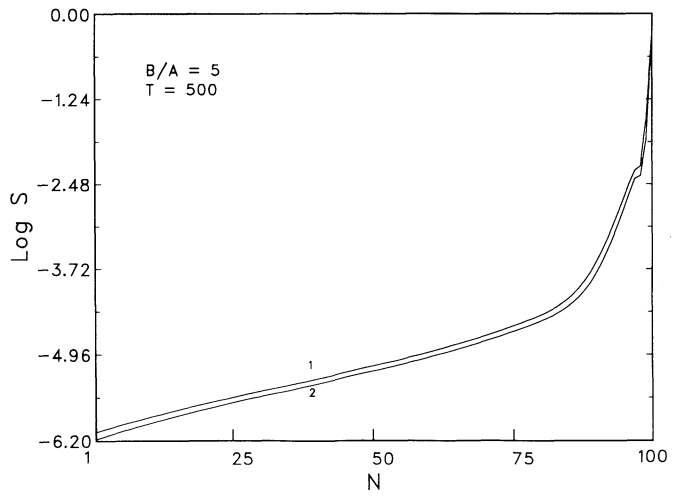

FIG. 7a

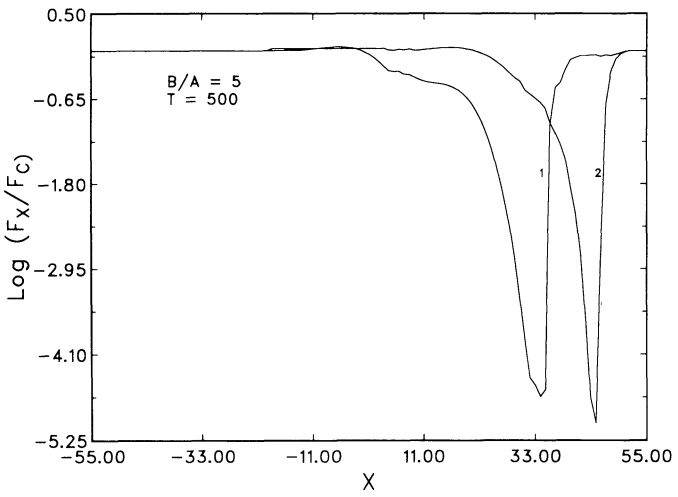

FIG. 7b

FIG. 7.—(*a*) Source functions according to the velocity laws given in eqs. (53) and (54). (1) $\alpha = -1$, (2) $\alpha = 0.9$. (*b*) Line profiles corresponding to the source functions given in (*a*).

and

$$\omega = 0.01 + 0.99\left(1 - \frac{1}{x}\right)^{\beta}, \tag{54}$$

where $v(r)$ is the velocity at the radius r, v_t is the terminal velocity, $\omega = v/v_\infty$, and $x = r/A$, where A is the photospheric radius or the inner radius of the spherical shell. We plotted the source function in Figures 7*a* and 9*a* for (1) $\alpha = -1$ and (2) $\alpha = 0.9$ in equation (49). We set $\beta = 1$. The corresponding line profiles are given in Figure 7*b*. Here we have put $V(r = A) = V_A = 0$ and $V(r = B) = V_B = 50$ mtu. In Figure 8*a* we plotted the source function for $V_A = 50$ mtu and $V_B = 1$ mtu. This represents a decelerating outward wind. The corresponding profiles are given in Figure 8*b*. In Figure 9*a* the source functions correspond to $V_A = 0$, $V_B = 50$ mtu, with discontinuity at shell numbers 51–59, where $V = 0$. The corresponding profiles are plotted in Figure 9*b*. The two velocity laws given in equations (49) and (50) appear to produce similar values of $\bar{S}$ and line profiles. Therefore, we felt that it is not necessary to show these separately. In Figure 10*a* we present the quantities $\bar{S}$ for $B/A = 5$, $T = 1300$, $T_e = 3 \times 10^4$ K, and $V = 10{,}000$–5000 km s^{-1} and the corresponding line profiles are given in Figure 10*b*. We notice that changes in the source function are between 80% and 100% at the emergent side of the medium. As the velocity increases we obtain narrow and deeper absorption lines (see Fig.10*b*). In Figure 11*a* we plotted values of $\bar{S}$ for $B/A = 10$ and $T = 500$. Again the source function changes considerably, as do the line profiles (Fig. 11*b*). In Figures 12*a*, 12*b*, 13*a*, and 13*b* we presented the results for different optical depths and the aspect ratios B/A.

This method, described in § 2, can handle the problems arising out of the coupling of the comoving points across the line profile and the local velocity gradients. The solution is calculated on the basis of the discrete space theory, which depends on the interaction principle (see Peraiah 1984) which connects the physical properties of the medium (such as scattering, large-scale motions, etc.) with

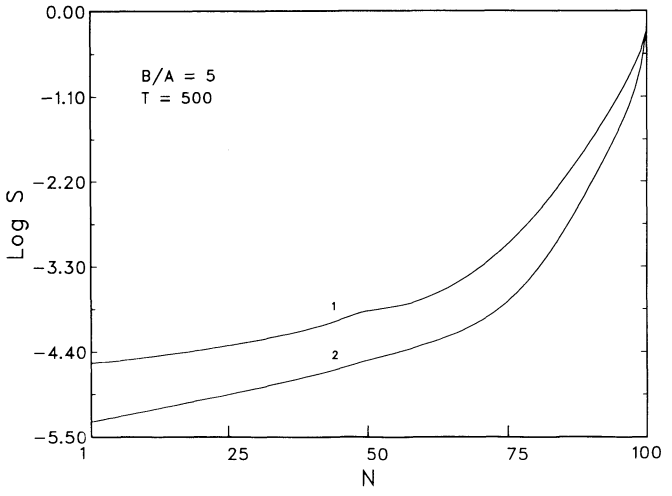

FIG. 8a

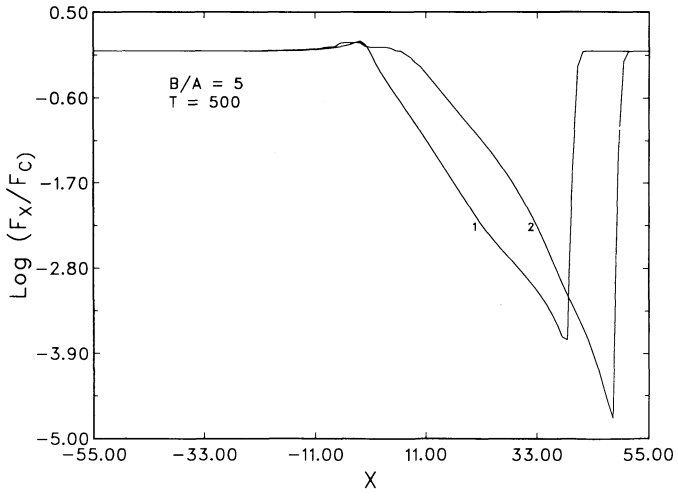

FIG. 8b

FIG. 8.—(*a*) Same as Fig. 7*a*, but with $V_A = 50$ mtu and 1 mtu. (*b*) Line profiles corresponding to the source functions given in (*a*).

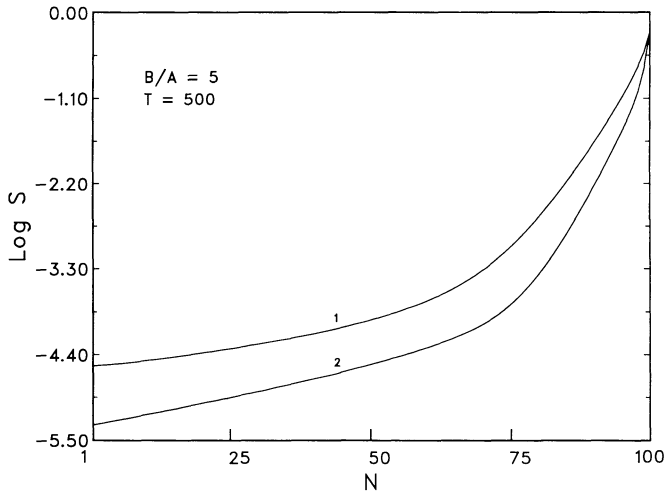

FIG. 9*a*

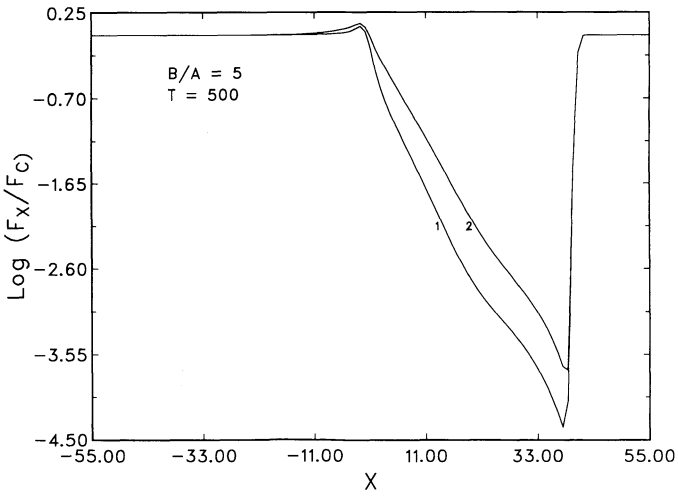

FIG. 9*b*

FIG. 9.—(*a*) Same as Fig. 7*a*, but with discontinuity at shells 51 and 59. (*b*) Line profiles corresponding the source functions given in (*a*).

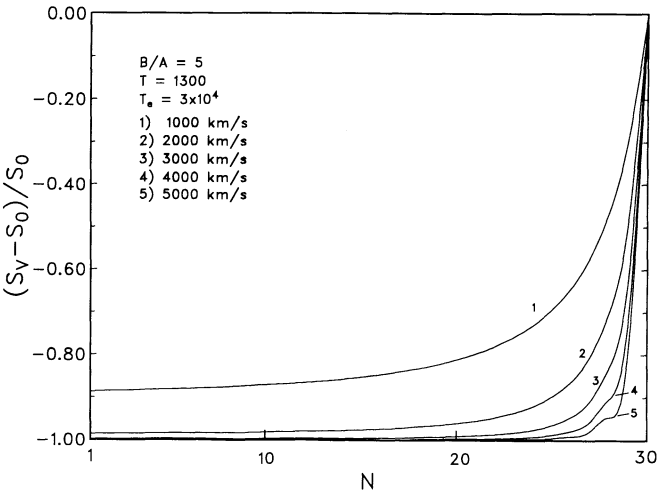

FIG. 10

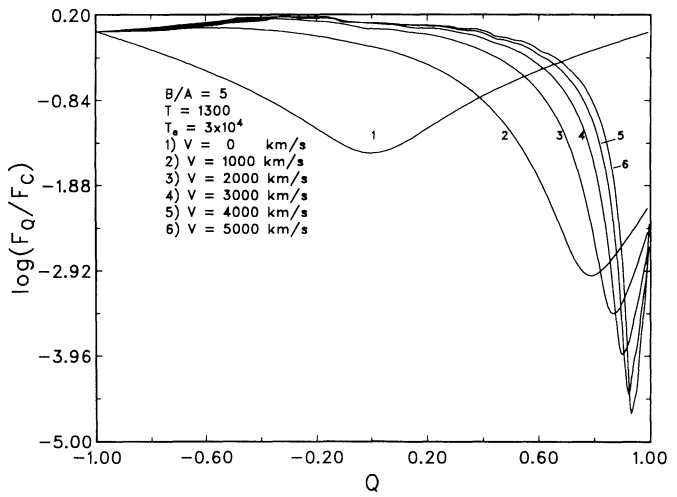

FIG. 10*b*

FIG. 10.—(*a*) $\bar{S}$ vs. N. (*b*) Line profiles corresponding to the source functions given in (*a*).

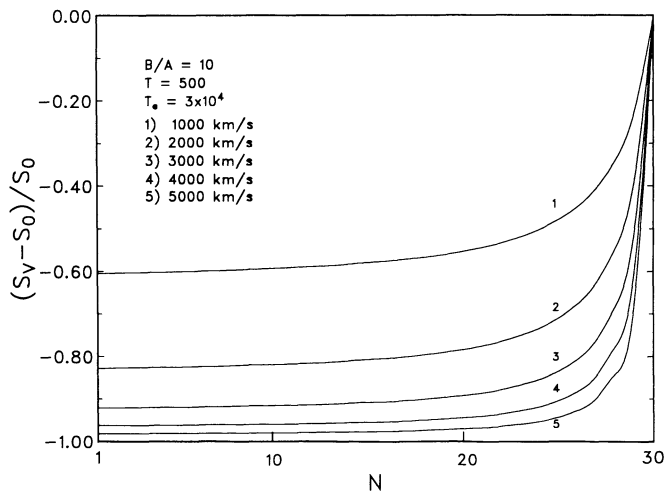

FIG. 11*a*

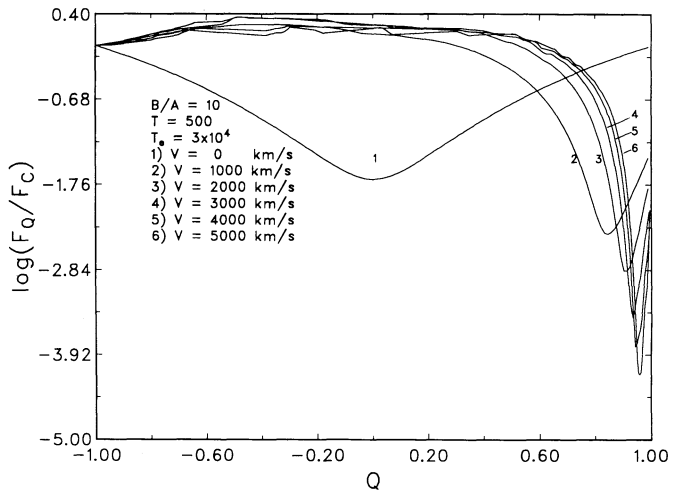

FIG. 11*b*

FIG. 11.—(*a*) $\bar{S}$ vs. N. (*b*) Line profiles corresponding to the source functions given in (*a*).

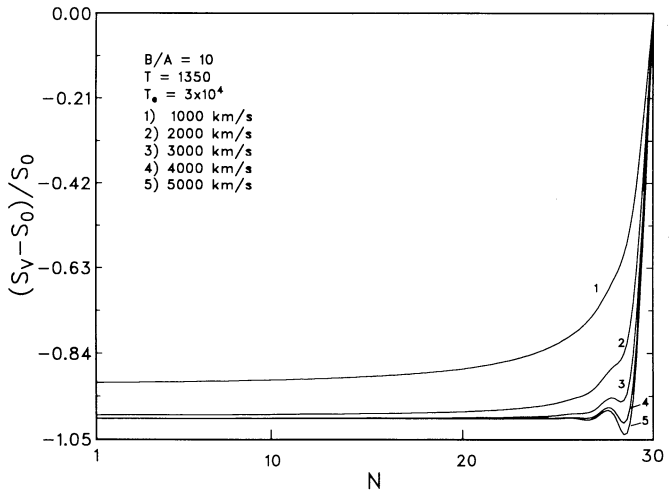

FIG. 12*a*

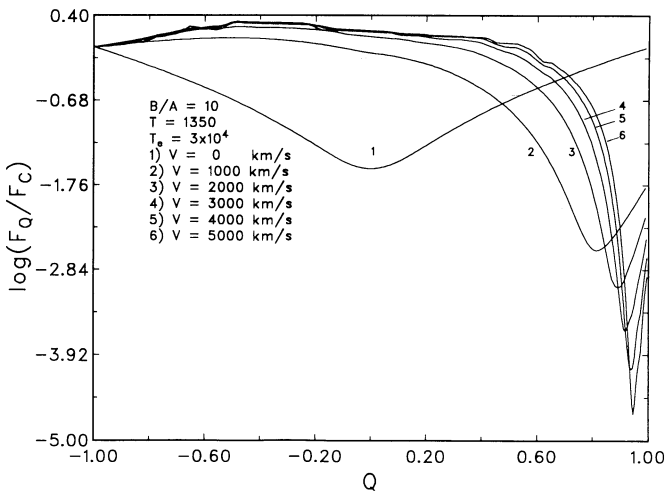

FIG. 12*b*

FIG. 12.—(*a*) $\bar{S}$ vs. N. (*b*) Line profiles corresponding to the surface source functions given in (*a*).

the transmitting and reflecting characteristics of the medium. The stability of the solution is achieved by controlling the step size which arises in the discretization in radial, angle, and frequency integrations. The step size is coupled to the physical conditions of the medium (see Peraiah 1980a). The critical step size is derived so that the transmission and reflection functions estimated in the given shell or layer are always positive and satisfy the conservation principles. Therefore, any inhomogeneity due to the changing physical conditions can be easily introduced into the critical step size. The actual size of the critical step size is to be determined according to the physical conditions in the shell, so that a stable and unique solution is obtained. In the present calculations we find that each shell (we divided into 30 shells) is represented by several mtu of velocity. Therefore, we subdivide each shell so that the step size is less than the critical step size which is used to calculate the transmission and reflection properties in this basic shell. By means of the "star algorithm" we combine all the basic shells and calculate the transmitting and reflecting properties of the compound shell. This again is subjected to conditions of stability and conservation. This ensures that the physical properties of the medium are properly taken care of. Finally, we use the internal field algorithm (Peraiah 1984) to estimate the diffuse radiation field. This way we maintain both the stability and the uniqueness of the solution, but also the conservation of radiative flux, which characterizes an important class of problems in radiative transfer theory.

4. CONCLUSIONS

The effects of aberration and advection in fast-moving fluids generate sufficiently large changes in the source function and the line profiles formed in such media. The high velocities of expansion reduce the emergent source functions by orders of magnitude, depending upon the geometrical extensions and line-center optical depths.

I would like to thank B. A. Varghese for help in the computations, and the referee, whose comments helped to improve the quality of the paper's contents greatly.

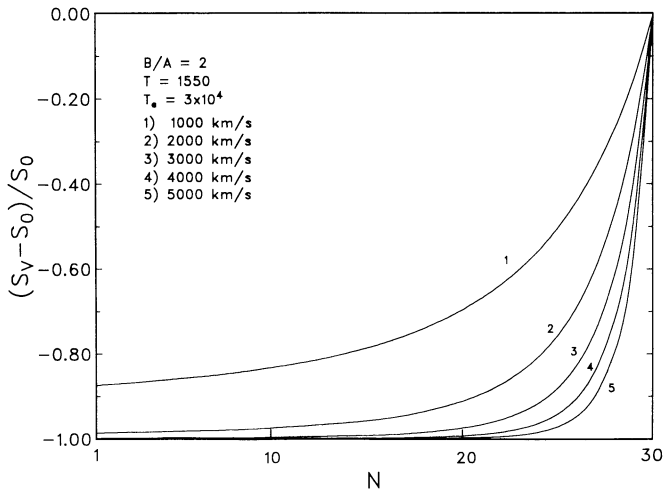

FIG. 13*a*

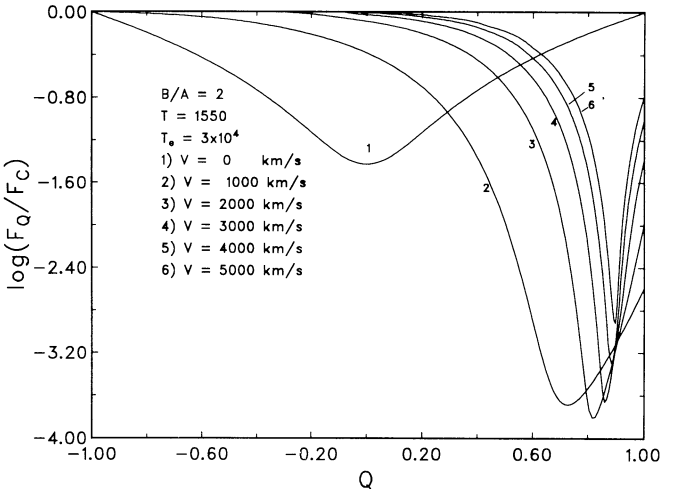

FIG. 13*b*

FIG. 13.—(*a*) $\bar{S}$ vs. N. (*b*) Line profiles corresponding to the source functions given in (*a*).

REFERENCES

Castor, J. I., & Lamers, H. J. G. L. M. 1979, ApJS, 39, 481
Grant, I. P., & Peraiah, A. 1972, MNRAS, 160, 239 (GP)
Lucy, L. B. 1971, ApJ, 163, 95
Mihalas, D., Kunasz, P. B., & Hummer, D. G. 1975, ApJ, 202, 465
———. 1976, ApJ, 206, 515
Peraiah, A. 1980a, Acta Astr., 30, 525
Peraiah, A. 1980b, J.Ap.Astr., 1, 3
———. 1984, in Methods in Radiative Transfer, ed. W. Kalkofen (Cambridge: Cambridge Univ. Press)
———. 1987, ApJ, 317, 271 (Paper I)
———. 1991, ApJ, 371, 673